

# Detection of 125.5-day Optical Periodic Modulation of the Neutron Star M51 ULX-8

S. Allak,<sup>1,2</sup>★

<sup>1</sup>*Department of Physics, University of Çanakkale Onsekiz Mart, 17100, Çanakkale, Türkiye*

<sup>2</sup>*Space Science and Solar Energy Research and Application Center (UZAYMER), University of Çukurova, 01330, Adana, Türkiye*

Accepted XXX. Received YYY; in original form ZZZ

## ABSTRACT

Studying Ultraluminous X-ray sources (ULXs) in the optical wavelengths provides important clues about the accretion mechanisms and the evolutionary processes of X-ray binary systems. In this study, three (C1, C2, and C3) possible optical counterparts were identified for well-known neutron star (NS) candidate M51 ULX-8 through advanced astrometry based on the *Chandra* and Hubble Space Telescope (*HST*) observations, as well as the *GAIA* optical source catalogue. Optical periodic modulation of 125.5 days with an amplitude of 0.14 magnitude was determined for C3 which has evidence to represent the optical nature of ULX-8 using one-year (2016–2017) 34 *HST* ACS (Advanced Camera for Surveys)/WFC (Wide Field Camera) observations. Moreover, surprisingly, the observed optical fluxes of C3 exhibit a bi-modal distribution. This could mean that there is a possible correlation between the optical and the X-ray flux variabilities of the ULX-8. The possible scenarios which are frequently mentioned in the literature proposed for the nature of optical emission and optical super-orbital period. The most probable scenario is that the optical emission could have originated from the accretion disk of the ULX-8.

**Key words:** galaxies: individual: M51 ULX-8 - X-rays: binaries - Optical counterparts of M51 ULX-8

## 1 INTRODUCTION

Ultraluminous X-ray sources (ULXs) are non-nuclear point-like extragalactic sources with an isotropic X-ray luminosity ( $L_X > 10^{39}$  erg s<sup>-1</sup>) are exceeding the Eddington limit for a typical  $10M_\odot$  stellar-mass black hole (sMBH) (Kaaret et al. 2017). Many studies were presented evidence of intermediate mass black holes (IMBHs,  $10^2$ – $10^5 M_\odot$ ) with accreting at sub-Eddington rates for the compact nature of ULX systems (Colbert & Mushotzky 1999; Miller et al. 2004; Roberts 2007; Sutton et al. 2012; Caballero-García et al. 2013; De Marco et al. 2013).

Thanks to the new-generation of X-ray observatories (e.g. *XMM-Newton*, *Chandra*, *NuSTAR*), the nature of ULXs has been further studied and a new perspective has been developed including accreting scenarios at super-Eddington limit for a sMBHs (Walton et al. 2014; Middleton et al. 2015; Walton et al. 2018). The discovery of a NS ULX (or pulsar ULX, PULX) in M82 by Bachetti et al. (2014) led us to change our perspective on the nature of ULXs. It is also exciting evidence that highly super-Eddington accretion can occur for sMBHs. Thrilling discoveries of PULXs continued in the followed years (Fürst et al. 2016; Israel et al. 2017a,b; Carpano et al. 2018; Sathyaprakash et al. 2019; Rodríguez Castillo et al. 2020). Moreover, a cyclotron resonance scattering feature (CRSF) in the X-ray spectrum of M51 ULX-8 was discovered (Brightman et al. 2018; Middleton et al. 2019a). This feature which is directly related to the measurement of the magnetic field indicates the presence of

a strong NS candidate in the ULX-8 system. Also very recently, the CRSF with the highest energy known to date was detected for the first Galactic PULX candidate Swift J0243.6+6124 by Kong et al. (2022).

Understanding the nature of the high luminosity mechanism and the compact objects (NSs or black holes, BHs) are the main purposes of ULXs studies. For this, X-ray-optical spectral and temporal analysis are very important tools. To determine possible optical counterpart(s) of ULXs, *Chandra* X-ray and *HST* optical observations which have high spatial resolution and positional accuracy usually are used. The number of detectable optical counterparts are quite limited since they are generally faint in the V-band ( $m_V \geq 21$  mag). Moreover, they are located in the fields of crowded and star clusters. Therefore, the number of ULXs that have unique possible optical counterparts are not exceed 30 (Tao et al. 2011; Gladstone et al. 2013).

Optical analysis provides precious clues of the nature of the donor star and disk geometry. In addition, this is a very useful tool in determining the masses of compact objects (Kaaret et al. 2017). However, the nature of optical emission of ULXs is still unclear. In other words, the optical emission could be originated from an accretion disk, a donor star or a combination of both. All these possibilities make it difficult for us to understand their optical nature. On the other hand, there have been many studies to identify and understand the nature of the possible optical counterpart(s) of ULXs. For instance, Liu et al. (2002); Kaaret et al. (2004) and Soria et al. (2005) reported that the high UV/optical magnitudes or blue colors of possible optical counterparts may be clues for OB-type stars. As a specific example, Motch et al. (2014) showed that photospheric

★ E-mail: 0417allaksinan@gmail.com

absorption lines were detected from the donor star in the blue part of the spectrum in NGC 7793 P13. However, [Fabrika et al. \(2015\)](#) pointed out that the He II line observed in NGC 7793 P13 must be formed in a photoionized wind from the accretion disc. On the other hand, the near-infrared counterparts of ULXs studies suggest that they may be red supergiants ([Heida et al. 2016](#); [López et al. 2020](#)). Moreover, the optical emission could be contaminated or dominated from an irradiated accretion disk ([Patruno & Zampieri 2008](#); [Grisé et al. 2012](#); [Sutton et al. 2014](#); [Yao & Feng 2019](#)).

The optical emission may originate from the photosphere of the wind at very high accretion rates with from irradiation of the donor star or together in some combination with the irradiated outer disk ([Middleton et al. \(2022\)](#) and references therein). Moreover, for the first time the far-UV emission from the NGC 6946 ULX source was detected by [Kaaret et al. \(2010\)](#) and they argued that it was a combination of disk emission and contribution from the donor star. In addition, Galactic super-Eddington accretor SS 433 which widely expected to be ultraluminous in the UV band ([Poutanen et al. 2007](#)) has shown optical spectra which associated with the emission from the outer photosphere ([Poutanen et al. 2007](#)). In addition, the optical line luminosity limits combined with the X-ray variability may allow for beaming factors of a typically less than an order of magnitude. This is compatible with a model for super-critical accretion and large scale height winds ([Begelman et al. 2006](#)).

The galaxy M51 (NGC 5194) and its companion NGC 5195 are a pair of interacting galaxies at a distance of 9 Mpc ([Song et al. 2020](#)). This galaxy hosts a large number of ULXs ([Terashima et al. 2006](#); [Swartz et al. 2011](#)). One of them is the well-known NS ULX-8. Figure 1 shows the location of the ULX-8 on a three-color (red, green and blue; RGB) mosaic image of *SDSS* (Sloan Digital Sky Survey). This present work focuses on possible optical counterparts of M51 ULX-8. Primary goal is to search for potential optical counterparts for ULX-8 by deploying one-year *HST* ACS/WFC F606W and F814W observations. It is also an important part of this study to investigate in detail the nature of long-term optical and also X-ray variability.

The paper is organized as follows: in section 2, data reduction and analysis (astrometric calculations, long-term optical variability, color magnitude diagrams and spectral energy distributions) are described. In section 3, Results of the optical analysis, astrometry, long-term optical variability of counterparts and concluding main findings are presented.

## 2 OBSERVATIONS, DATA REDUCTION AND ANALYSIS

### 2.1 Observations

The M51 galaxy was observed many times by the *HST* and *Chandra* observatories. The main *HST* observations presented in this study are 34 drizzled images which were taken between 2016 and 2017 (Proposal ID 14704). These observations were obtained using the *HST* ACS F606W and F814W filters with the same exposure time of 2200 seconds (s). In addition, 2005-01-20 *HST*/ACS F435W (B-band), F555W (V-band) and F814W (I-band) drizzled images with exposure times of 2720 s, 1360 s, 1360 s, were also used to obtain for the color magnitude diagrams (CMDs) and spectral energy distributions (SEDs). Furthermore, archived 21 *Chandra* X-ray observations of ULX-8 (Table 1) were used for astrometric calculations as well as for X-ray temporal analysis.

### 2.2 Determination of Optical Counterparts

In previous work, [Terashima et al. \(2006\)](#) performed astrometry to determine the optical counterpart of M51 ULX8. In their work, point-like sources in the ACS images compared with sources in the 2MASS (Two Micron All Sky Survey) catalog. They found systematic offsets for R.A (right ascension) and for Decl. (declination) and they shifted the ACS images to the 2MASS positions. After this alignment, they determined four reference sources between ACS and *Chandra* images. As a result, they derived the astrometric error radius as  $0''.3$  at 90% confidence between *Chandra* and *HST* images (see for more details [Terashima et al. \(2006\)](#)).

Using a different approach from the [Terashima et al. \(2006\)](#), the possible optical counterparts of the M51 ULX-8 were investigated as described follows: Optical counterparts of ULX sources could be determined by precise astrometric calculations using *HST* and *Chandra* observations, which generally have very good spatial resolution. Initially, the archive data sets from *HST* and *Chandra* were used to determine the possible optical counterparts of neutron star M51 ULX-8. For this, possible reference sources were searched by comparing 21 *Chandra* ACIS-S X-ray observations with *HST* ACS/F606W and F814W optical observations. The, *wavdetect* tool in *CIAO* and the *daofind* task in *DAOPHOT/IRAF* tasks were used for source detection in *Chandra* and *HST* observations, respectively. An align problem was noticed especially in *HST* ACS/F606W and F814W as well as *Chandra* observations. The *Chandra* observations were aligned by cross-matching another *Chandra* observation (ObsID 23478), which provided a relative correction. For these processes, *wcsmatch* and *wcsupdate* tools in *CIAO* were used. The *imalign* tool in *IRAF* was run to equalize the relatively large shifts in the W606W and F814W observations. However, for precision astrometry between *Chandra* and *HST* data sets, adequate reference sources were not found. Therefore, *GAIA* source catalog was used for astrometric calculations.

Since ds9 (An image display and visualization tool for astronomical data, [Joye & Mandel 2003](#)) already has an interface to various standard catalogues it was used to retrieve data from the *GAIA* catalogue. From this catalogue, the reference sources which appear to be isolated and point-like in *Chandra* and *HST* images were searched. Considering also the shift directions of matched sources, four reference sources were found between both *Chandra*-*GAIA* and *GAIA*-*HST*. Of course, there were more than four reference sources between *GAIA*-*HST*, but they were not affected the results since the values of shift as well as shift directions were the same. The coordinates of all identified reference sources are shown in Figure 2. In particular, the same shift direction of the reference sources between *Chandra* and *GAIA* indicates that the selected sources are the accurate references (see the left panel of Figure 2). The astrometric offsets between *Chandra* and *GAIA* were found as  $-0''.83 \pm 0''.07$  for R.A and  $-0''.72 \pm 0''.33$  for Decl. with  $1-\sigma$  errors and also astrometric offsets between *GAIA* and *HST* were found as  $-0''.07 \pm 0''.03$  for R.A and  $-0''.04 \pm 0''.02$  for Decl. with  $1-\sigma$  errors. The total astrometric errors between *Chandra*-*GAIA* and between *GAIA* -*HST* were derived as  $0''.33$  and  $0''.03$ , respectively. The calculation to determine the final optical coordinates of the ULX-8 is described in equations (1), (2) and (3):

$$IC = IG \pm \Delta R.A.(IC-IG) \pm \Delta Decl.(IC-IG) \quad (1)$$

$$IG = IH \pm \Delta R.A.(IG-IH) \pm \Delta Decl.(IG-IH) \quad (2)$$

Where the *Chandra*, *GAIA* and *HST* images are described as IC, IG and IH, respectively.  $\Delta R.A$  and  $\Delta Decl.$  are average shifts of R.A

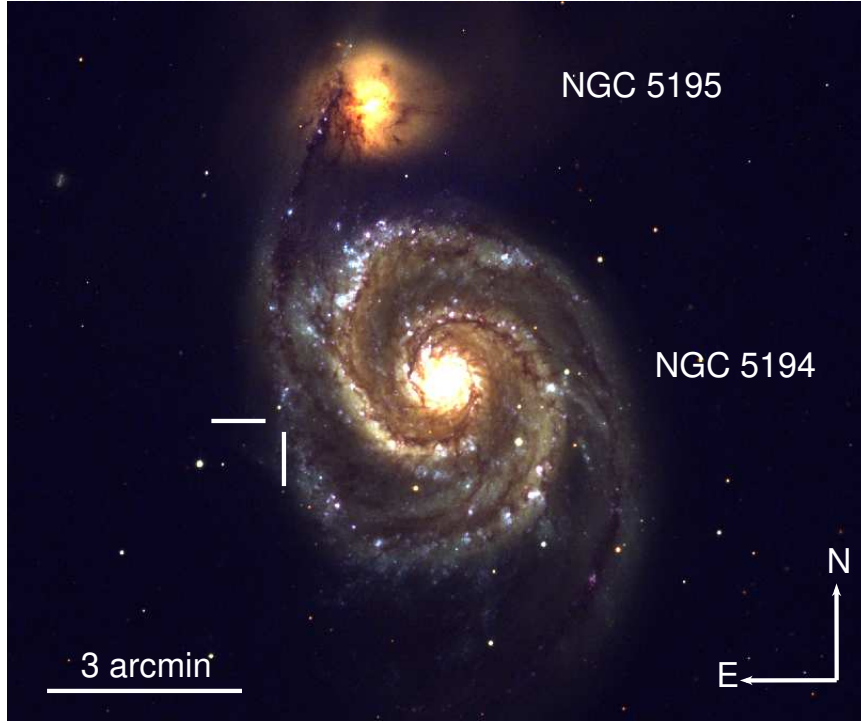


**Figure 1.** RGB *SDSS* mosaic image of the M51 (NGC 5194/5194) galaxy. The white bars represent the position of ULX-8.

**Table 1.** *chandra* X-ray observations log for M51 ULX-8

ObsID	Instrument	Date (YYYY-MM-DD)	Exp. (ks)	$F_X^a$ ( $\text{erg cm}^{-2} \text{s}^{-1}$ )	$L_X^b$ ( $\text{erg s}^{-1}$ )
354	ACIS-S	2000-06-20	14.86	$3.79 \pm 0.21$	$3.67 \pm 0.20$
1622	ACIS-S	2001-06-23	26.81	$2.28 \pm 0.12$	$2.21 \pm 0.12$
3932	ACIS-S	2003-08-07	47.97	$3.25 \pm 0.12$	$3.15 \pm 0.12$
12562	ACIS-S	2011-06-12	9.63	$6.42 \pm 0.39$	$6.22 \pm 0.38$
12668	ACIS-S	2011-07-03	9.99	$3.34 \pm 0.27$	$3.24 \pm 0.26$
13813	ACIS-S	2012-09-09	179.20	$5.80 \pm 0.09$	$5.62 \pm 0.09$
13812	ACIS-S	2012-09-12	157.46	$4.19 \pm 0.08$	$4.06 \pm 0.08$
15496	ACIS-S	2012-09-19	40.97	$3.49 \pm 0.14$	$3.38 \pm 0.14$
13814	ACIS-S	2012-09-20	189.85	$3.20 \pm 0.06$	$3.10 \pm 0.06$
13815	ACIS-S	2012-09-23	67.18	$3.23 \pm 0.11$	$3.13 \pm 0.11$
13816	ACIS-S	2012-09-26	73.10	$3.80 \pm 0.11$	$3.68 \pm 0.11$
15553	ACIS-S	2012-10-10	37.57	$4.43 \pm 0.17$	$4.29 \pm 0.16$
<i>19522</i>	ACIS-I	2017-03-17	37.76	$1.39 \pm 0.13$	$1.35 \pm 0.13$
<i>20998</i>	ACIS-S	2018-08-31	19.82	$5.18 \pm 0.29$	$5.02 \pm 0.28$
<i>23472</i>	ACIS-S	2020-10-13	33.62	$2.35 \pm 0.17$	$2.28 \pm 0.16$
<i>23473</i>	ACIS-S	2020-11-18	34.51	$2.67 \pm 0.19$	$2.59 \pm 0.18$
<i>23474</i>	ACIS-S	2020-12-21	36.14	$8.10 \pm 0.31$	$7.85 \pm 0.30$
<i>23475</i>	ACIS-S	2021-01-28	34.51	$8.86 \pm 0.35$	$8.58 \pm 0.34$
<i>23476</i>	ACIS-S	2021-03-01	34.44	$10.20 \pm 0.33$	$9.88 \pm 0.32$
<i>23477</i>	ACIS-S	2021-04-01	31.64	$3.38 \pm 0.21$	$3.27 \pm 0.20$
<i>23478</i>	ACIS-S	2021-05-04	31.55	$11.30 \pm 0.40$	$10.95 \pm 0.39$

Notes: <sup>a</sup> and <sup>b</sup> represent unabsorbed flux and luminosity in units of  $10^{-13} \text{ ergs cm}^{-2} \text{ s}^{-1}$  and  $10^{39} \text{ ergs s}^{-1}$  with  $1-\sigma$  errors, respectively. ObsIDs in *italics* indicate previously unused data for ULX-8.

and Decl., respectively. The plus-minus signs,  $\pm$ , depend on the shift directions. To simplify, the last two terms of the equation (1) and equation (2) were called A and B respectively. The equation (3)

gives the X-ray position of ULX-8 on the astrometric-corrected *HST* images.

$$IC = IH \pm A \pm B \quad (3)$$

Finally, accepted  $1-\sigma$  accuracy in *Chandra* position as  $0''.1$ , the

positional error radius of ULX-8 was derived as  $0''.58$  at 90% confidence level by combined all errors in quadrature. The *Chandra* X-ray position of the M51 ULX-8 on the astrometric-corrected *HST*/WFC F606W and F814W images are displayed in Figure 3. In the astrometric error radius, three discrete optical sources which have FWHM (The full Width at Half Maximum) as  $\geq 5$  pixels ( $0''.25$ ) were identified. According to increasing R.A values of these sources are labeled as C1, C2 and C3 and the *HST* optical coordinates of possible optical counterparts are given in Table 2.

### 2.3 Photometry of Possible Optical counterparts

For all drizzled images, point-like sources were detected with the *daofind* task and aperture photometry of these sources was performed using the *APPHOT* package in *IRAF*. To perform photometry, 3 pixels ( $0''.15$ ) aperture radius was chosen. In order to obtain photometric errors and data quality propagation, the pixel values were multiplied by the exposure time using *imarith* tool in *IRAF*. The Vega magnitudes were derived instrumental magnitudes using ACS/WFC zero point magnitudes from Sirianni et al. (2005). To derive the aperture corrections with a radius between 3 pixels to 10 pixels for each image using 30 isolated and bright sources. The obtained Vega magnitude values were corrected with the foreground dust-extinction  $A_V = 0.46$  mag. from Allak et al. (2022a). The dereddened Vega magnitudes of the possible optical counterparts are given in Tables 2 and 3.

In addition, the PSF (Point Spread Function) was performed to derive photometry following the similar approach given by Allak et al. (2022a). 30 bright and isolated sources near the optical counterparts were selected to build the PSF model using the *DAOPHOT* package Stetson (1987) in *IRAF*. PSF fitting radius was taken as 3 pixels in the *allstar* task. The optical counterparts are discrete sources which are convenient for aperture photometry. In addition, in terms of their magnitudes there are no dramatic differences between the two methods therefore, only the results of aperture photometry are presented here.

### 2.4 Color-Magnitude Diagrams & Spectral Energy Distributions

To classify possible optical counterparts, C1, C2 and C3,  $F_X/F_{optik}$  ratios were derived using equation (5) which given by Maccacaro et al. (1982):

$$\log(F_X/F_{optik}) = \log(F_X) + m_V/2.5 + 5.37 \quad (4)$$

Here, the  $F_X$  is observed absorbed flux obtained from a simple *power-law* in the 0.3–3.5 keV energy range and  $m_V$  is the V-band magnitude. Since there were no simultaneous *Chandra* and *HST* V-band observations, nearly simultaneous Mar. 17, 2017 (MJD: 57829.03334) *Chandra* and Mar. 21, 2017 (MJD: 57833.60502) *HST* F606W observations were used.  $F_X/F_{optik}$  ratios of C1, C2 and C3 were derived as  $2.58 \pm 0.03$ ,  $1.65 \pm 0.02$  and  $2.33 \pm 0.03$ , respectively. The  $F_X/F_{optik}$  value of C2 is in the range of AGNs (Active Galactic Nucleus) or BL Lac objects ( $-1$  to  $1.7$ ) (Stocke et al. 1991).

Investigating the environment (e.g. nearby stars or group of stars) of the ULX-8 could be a good tool to estimate the ages of its possible optical counterparts. In order to constrain the ages of the possible optical counterparts, CMDs were obtained using the colours of nearby stars of ULX-8 and counterparts. For this, similar colour values of possible optical counterparts and field stars were chosen. CMD, V-band versus B–V colours were derived for optical counterparts and

the nearby field stars. PARSEC (Bressan et al. 2012) isochrones were generated using the metallicity of  $Z=0.015$  (Urquhart et al. 2018) and  $A_V=0.46$  mag. The distance modulus was derived as 29.7 mag. using a distance of 9 Mpc. The CMD of C1 and C3 are displayed in Figure 4. According to resultant CMD, the age ranges of C1 (black triangle) and C3 (black square) could be constrained to  $\sim 90$  Myr for C1 and (18–30) Myr for C3.

Spectral energy distributions (SEDs) of the possible optical counterparts constructed to obtain the possible spectral characteristics of ULX-8 using the derived flux values B-band, V-band, I-band and also F606W filter. For SED plots, the pivot wavelengths of the ACS/WFC filters were selected. The optical SED for only counterpart C3 was adequately well-fitted with *power-law* model with a photon index,  $\alpha = -2.98 \pm 0.29$  at 95% confidence level. However, an acceptable model could not be obtained for the remaining C2 and C3. The  $\chi^2_\nu$  of *power-law* model for C1, C2 and C3 were found as 0.49, 1.89 and 0.84, respectively. In all cases, the number of degrees of freedom (dof) is two. The SEDs of all possible counterparts are displayed in Figure 5.

### 2.5 Temporal Analysis of Possible Optical Counterparts

The Vega magnitudes and associated and  $1-\sigma$  errors of possible optical counterparts of the ULX-8 in the F606W and F814W filters were listed in Table 3. In order to search for periodic variability of possible optical counterparts, the long-term light-curves were produced for each filter using all ACS/WFC observations. As seen in the light-curves in the lower panel of Figure 6, a sinusoidal shape was seen for candidate C3 albeit it was not observed for the C1 and C2. The standard deviation values ( $\leq 0.09$ ) of the C1 and C2 magnitudes are almost equivalent to their errors, this indicates that these sources do not have optical variations in the F606W and F814W filters. The F606W and F814W light-curves of C3 well-fitted a sinusoidal curve of equation (4) given by Liu et al. (2009):

$$m(t) = \bar{m} + A \sin[2\pi(t - t_I)/P + \phi] \quad (5)$$

From the best fitting of the F606W light-curve, a period ( $P$ ) was found as  $124.12 \pm 0.27$  days (d) with amplitude  $A = 0.14 \pm 0.02$  mag. at 95% confidence level. In case of F814W observations, the  $P$  and  $A$  were found as  $127.04 \pm 2.24$  d and  $0.11 \pm 0.02$ , respectively, at 95% confidence level. The reduced  $\chi^2$  values of the fitting F606W and F814W light-curves were 1.48 and 1.27, respectively. In both cases, the dof was 31. The well-fitted parameters ( $P$ ,  $A$ ,  $\bar{m}$  (average magnitude) and  $\phi$  (phase)) of both light-curves are given in Table 4.

Moreover, to check long-term periodicity, Lomb-Scargle (L-S) periodogram (Lomb 1976; Scargle 1982) which is a sub-package time series of the *Python/Astropy* was used. From the L-S periodogram,  $\sim 124$  d and  $\sim 127$  d periods were found with false alarm probability (FAP) as  $3.1 \times 10^{-3}$  and  $2.8 \times 10^{-2}$ , respectively (see Figure 7). In order to estimate the uncertainty on the periods a Monte Carlo simulation was used with *astropy uncertainty package*. Following the similar approach given by Drave et al. (2010) the 0.58 and 3.66 d at 95% confidence level errors were found for the 124 and 127 d periods of ULX-8, respectively. The final period and amplitude of C3 were derived as  $125.5 \pm 2.3$  d and  $0.14 \pm 0.11$  by averaged the values which were found from the sinusoidal curve and the L-S analysis.

Numerous X-ray binaries and AGNs may show persistent random modulations such as stochastic and red-noise since in their emission driven by the complex and turbulent accretion process (Vaughan



**Table 2.** The astrometric-corrected *Chandra* X-ray position of the M51 ULX-8 and Vega magnitudes of the possible optical counterparts C1, C2 and C3

Source.	<i>HST</i> R.A. (hh:mm:ss.sss)	<i>HST</i> Dec. (° : ' : ")	F435W mag. (Vega)	F555W mag. (Vega)	F814W Mag. (Vega)
ULX-8	13:30:07.64	+47:11:06.97	...	...	...
C1	13:30:07.60	+47:11:06.98	$26.90 \pm 0.18$	$26.08 \pm 0.17$	$25.72 \pm 0.07$
C2	13:30:07.62	+47:11:06.76	$23.90 \pm 0.04$	$24.01 \pm 0.06$	$24.77 \pm 0.06$
C3	13:30:07.65	+47:11:06.94	$26.17 \pm 0.07$	$26.22 \pm 0.06$	$26.03 \pm 0.05$

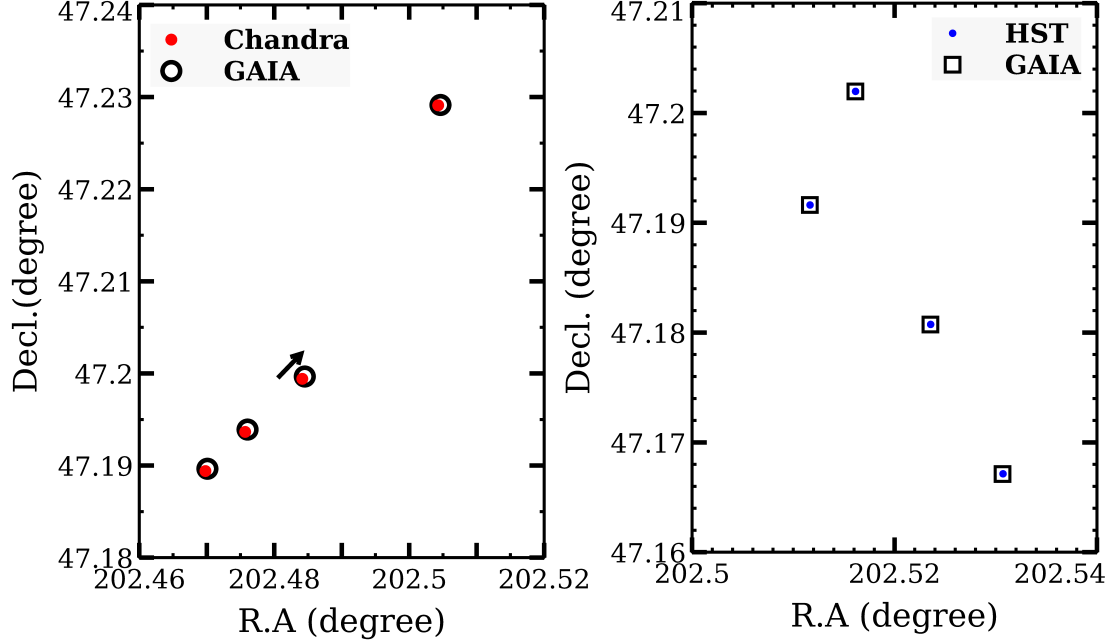


**Figure 2.** Coordinates of *Chandra* & *GAIA* (left) and *GAIA* & *HST* (right) reference sources used in astrometric calculations. In the left panel, *Chandra* X-ray and *GAIA* optical reference sources are represented by filled red and unfilled black circles, respectively. The shift directions of the reference sources are indicated with the black arrow. In the right panel, *GAIA* and *HST* optical reference sources are represented by unfilled black squares and filled blue circles, respectively.

et al. 2016). In order to search the probabilities of a false detection due to red-noise, the Monte-Carlo simulation was used following the procedure used by An et al. (2013, 2016). A total of 10000 simulated red-noise time series which have the same number of sampling points and the same parameters given in Table 4 were generated for each filter. This allows us to estimate high significance against possible false detection. To estimate the red-noise continuum the L-S is applied for each simulated light-curve with the *power-law* index ranging between -1 and -2 and with the multi-frequency. The simulated maximum power was not exceed the maximum power from the real data at 99.7% confidence level. This result supports the interpretation that the determined periodicity is not spurious. Moreover, the light-curves of all the optical counterparts are different this may indicates that the periodic modulation is not due to systematic error and the effects of background images.

In addition, the observed optical flux distributions for source C3 are displayed in Figure 8 using F606W (left) and F814W (right) observations. As seen in this figure, the source C3 showed evidence of bi-modal distributions. The fluxes are derived from the Vega magni-

tudes of both filters. For the flux calculations, pivot wavelengths and the flux densities were taken from the Sirianni et al. (2005).

Recently, new *Chandra* X-ray observations of galaxy M51 have been published (e.g. Earnshaw (2020)). To quick look at the nature of X-ray variability of ULX-8, in addition to new observations, almost published all *Chandra* data sets (Table 1) were used. In order to obtain the long-term X-ray light-curve of ULX-8, the observed unabsorbed X-ray fluxes derived using 21 *Chandra* observations (Table 1) in the energy range of 0.5-7 keV. For this, a generic spectral shape was assumed with a *power-law* photon index of  $\Gamma=1.7$  (Song et al. 2020) and a Galactic absorption component,  $N_H=0.03 \times 10^{22} \text{ cm}^{-2}$  using *srcflux* task in CIAO. For in input source and background regions, 8'' and 16'' radii were chosen, respectively. The minimum and maximum unabsorbed X-ray fluxes were derived as  $(1.40 \pm 0.13) \times 10^{-13}$  and  $(10.30 \pm 0.40) \times 10^{-13} \text{ erg cm}^{-2} \text{ s}^{-1}$ . Based on distance of galaxy M51 (9 Mpc) these fluxes correspond to X-ray luminosities as  $(1.35 \pm 0.13) \times 10^{39}$  and  $(10.95 \pm 0.39) \times 10^{39} \text{ erg s}^{-1}$ , respectively (see Table 1). The resulting X-ray light-curve of ULX-8 and its histogram are shown in the Figure 9. As seen in this figure, the source reached its peak flux values in recently published observations. There was no

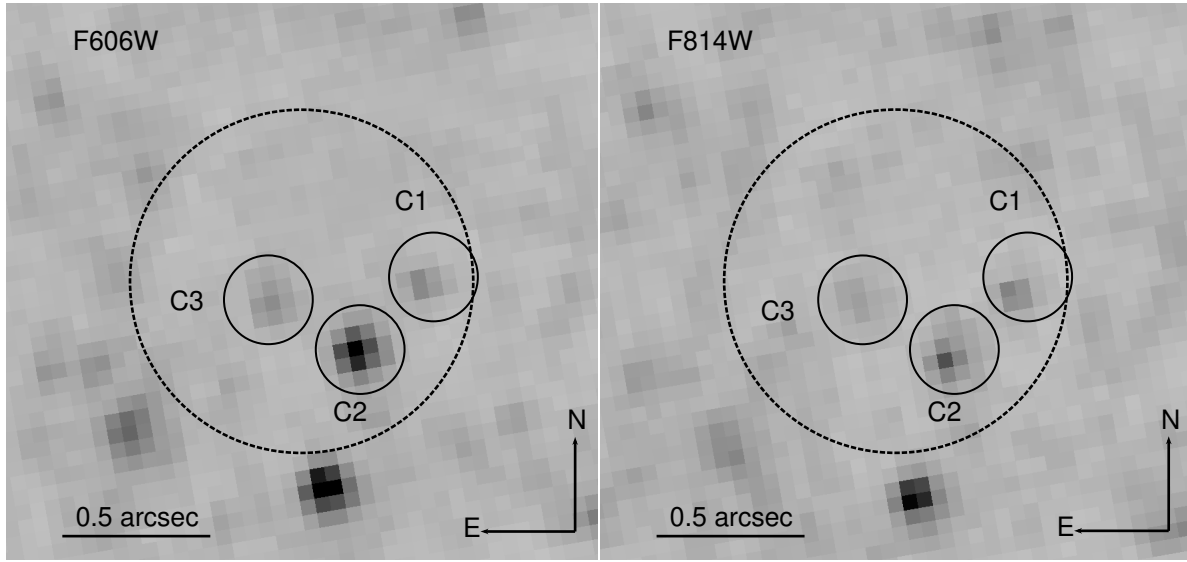


**Figure 3.** The *Chandra* X-ray position of the M51 ULX-8 on the astrometric-corrected *HST/WFC* F606W (left) and F814W (right) images. Black dashed circles indicate the astrometric error radius of  $0''.58$  around the X-ray position and solid black circles represent the center coordinates of each possible optical counterpart (C1, C2 and C3).

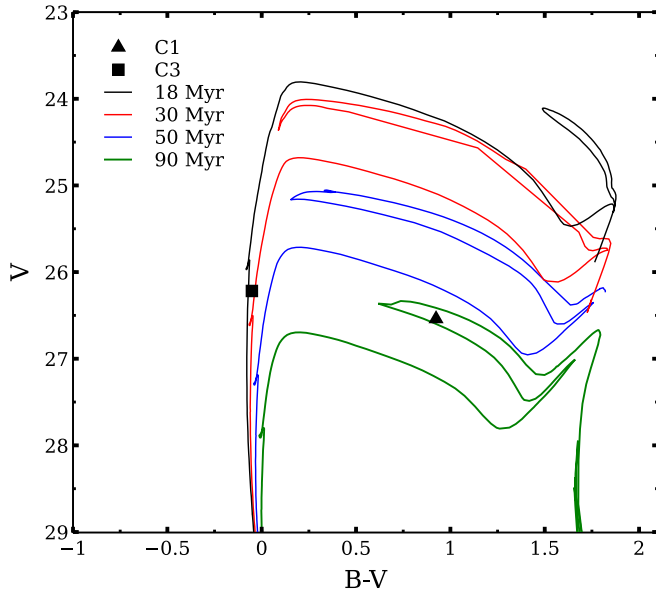


**Figure 4.** CMD of ULX-8, the black, red, blue and green solid colours represent the age (18-90 Myr) isochrones of C1 (filled black triangle) and C3 (filled black square). The isochrones were corrected for extinction of  $A_V = 0.46$  mag.

strong evidence of the bi-modality and any periodic modulation in the *Chandra* X-ray light-curve.

### 3 DISCUSSION & CONCLUSION

The main goal of this study, the precise optical positions of the neutron star M51 ULX-8 obtained via advanced astrometry based on the *Chandra* and *HST* observations as well as *GAIA* source catalogues. Examining all the optical images listed in Table 3 and also 2005-01-

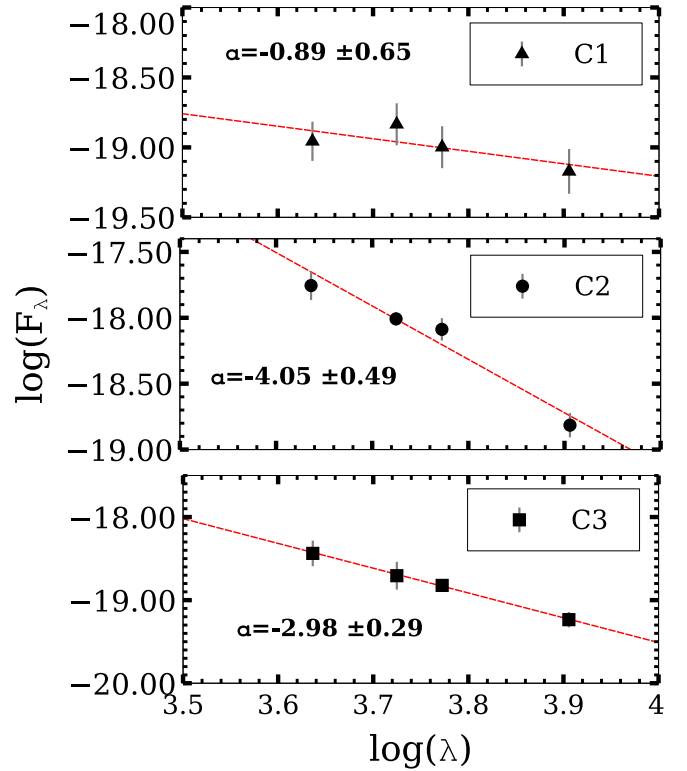


**Figure 5.** The reddening corrected SED of the possible counterparts of ULX-8. The *power-law* model is shown by dashed red lines. The source labels and model parameter are also denoted in the captions of each plot. The units of y and x axes are  $\text{erg cm}^{-2} \text{s}^{-1} \text{\AA}^{-1}$  and  $\text{\AA}$ , respectively.

20 *HST/ACS* F435W, F555W and F814W data sets, three discrete sources C1, C2 and C3 were identified within the astrometric error radius of  $0''.58$  at 90% confidence level. This result is different from the astrometric calculations given in Terashima et al. (2006). They

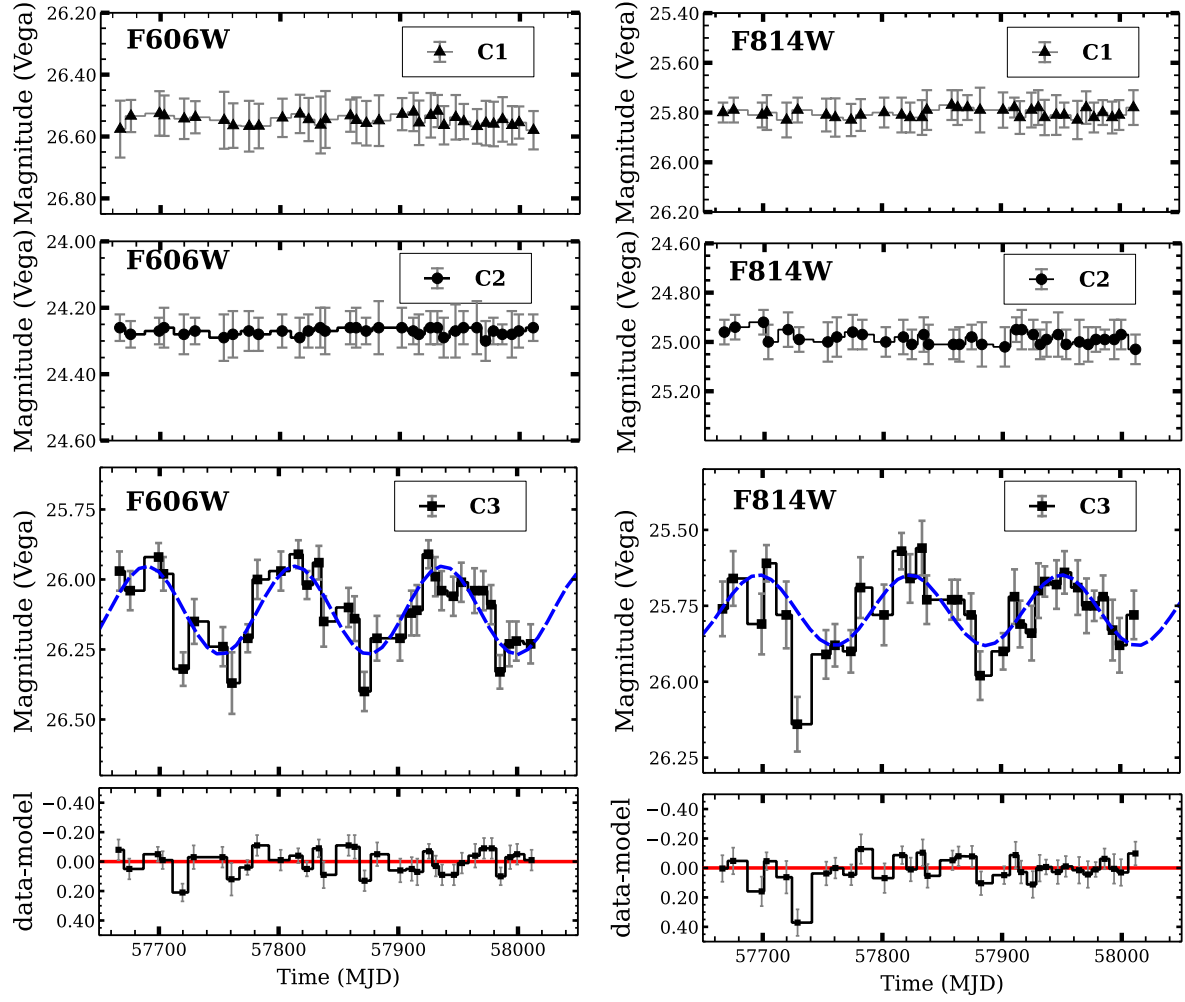


**Figure 6.** The light-curves of the possible optical counterparts C1 (upper), C2 (center) and C3 (lower) in the F606W and the F814W filters. For counterpart C3, sinusoidal fits are represented blue dashed lines and their residuals are shown the lower panels.

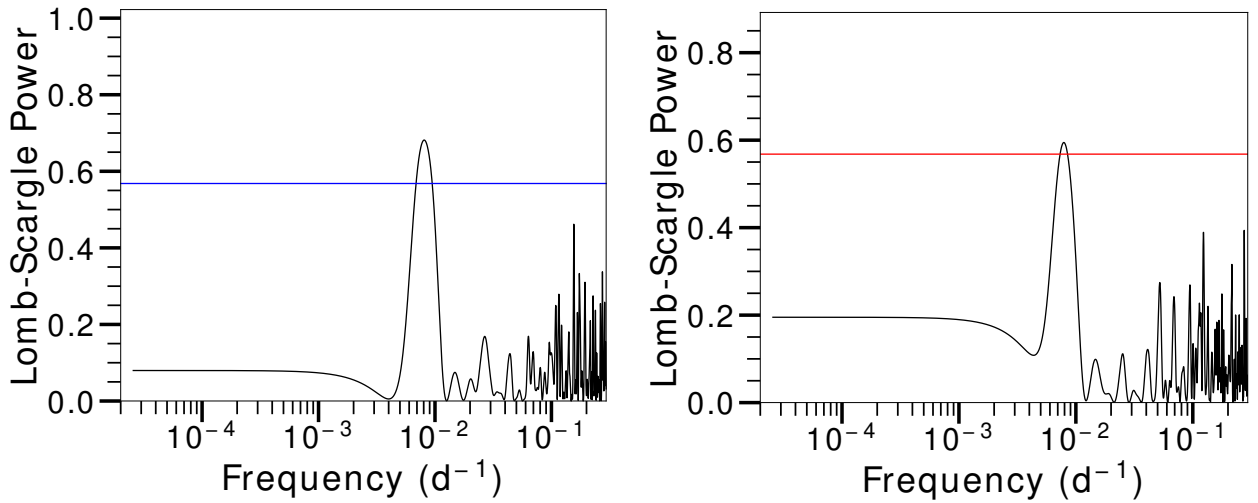


**Figure 7.** Lomb-Scargle periodograms of the F606W (left) and F814W (right) observations. Periodic signals that peak at 124 d and 127 d are found for the F606W (left) and F814W, respectively. The solid blue and red lines represent the 95% confidence level.

**Table 3.** Vega magnitudes of the possible optical counterparts C1, C2 and C3

Number (1)	F606W Vega Magnitudes				F814W Vega Magnitudes			
	Time (2)	C1 (3)	C2 (4)	C3 (5)	Time (6)	C1 (7)	C2 (8)	C3 (9)
1	57666.23008	26.58 ± 0.07	24.26 ± 0.04	25.97 ± 0.07	57666.29509	25.80 ± 0.04	24.96 ± 0.05	25.76 ± 0.09
2	57675.23803	26.53 ± 0.09	24.28 ± 0.04	26.04 ± 0.07	57675.30338	25.79 ± 0.05	24.94 ± 0.05	25.66 ± 0.09
3	57699.07316	26.53 ± 0.05	24.27 ± 0.04	25.92 ± 0.05	57699.13777	25.81 ± 0.05	24.92 ± 0.05	25.81 ± 0.10
4	57703.11242	26.53 ± 0.07	24.26 ± 0.06	25.98 ± 0.06	57703.17599	25.80 ± 0.07	25.00 ± 0.07	25.61 ± 0.06
5	57719.68466	26.54 ± 0.07	24.28 ± 0.06	26.32 ± 0.06	57719.77352	25.83 ± 0.07	24.95 ± 0.07	25.78 ± 0.11
6	57729.02204	26.54 ± 0.07	24.27 ± 0.04	26.15 ± 0.08	57729.10245	25.79 ± 0.05	24.99 ± 0.05	26.14 ± 0.09
7	57753.05545	26.55 ± 0.05	24.29 ± 0.07	26.24 ± 0.07	57753.12005	25.81 ± 0.07	25.00 ± 0.08	25.91 ± 0.08
8	57760.60783	26.56 ± 0.09	24.28 ± 0.07	26.37 ± 0.11	57760.68225	25.82 ± 0.08	24.98 ± 0.08	25.88 ± 0.07
9	57773.93019	26.57 ± 0.07	24.27 ± 0.06	26.21 ± 0.05	57773.99199	25.83 ± 0.06	24.96 ± 0.07	25.90 ± 0.07
10	57782.01584	26.57 ± 0.08	24.28 ± 0.05	26.00 ± 0.07	57782.09514	25.81 ± 0.06	24.97 ± 0.06	25.69 ± 0.10
11	57801.73972	26.54 ± 0.07	24.27 ± 0.05	25.97 ± 0.07	57801.80433	25.80 ± 0.06	25.00 ± 0.06	25.78 ± 0.10
12	57816.38990	26.53 ± 0.06	24.29 ± 0.06	25.91 ± 0.05	57816.50321	25.81 ± 0.07	24.98 ± 0.07	25.57 ± 0.06
13	57823.60626	26.55 ± 0.06	24.27 ± 0.05	26.02 ± 0.05	57823.67499	25.82 ± 0.06	25.01 ± 0.06	25.66 ± 0.08
14	57833.60502	26.56 ± 0.07	24.26 ± 0.06	25.94 ± 0.06	57833.66838	25.82 ± 0.07	24.97 ± 0.07	25.56 ± 0.09
15	57837.64349	26.54 ± 0.09	24.27 ± 0.07	26.15 ± 0.09	57837.70811	25.79 ± 0.08	25.01 ± 0.08	25.73 ± 0.08
16	57858.50069	26.53 ± 0.09	24.26 ± 0.05	26.10 ± 0.07	57858.56530	25.77 ± 0.06	25.01 ± 0.06	25.73 ± 0.07
17	57863.53201	26.55 ± 0.05	24.26 ± 0.06	26.14 ± 0.08	57863.59661	25.78 ± 0.07	25.01 ± 0.07	25.73 ± 0.07
18	57871.80715	26.56 ± 0.07	24.27 ± 0.04	26.40 ± 0.07	57871.87212	25.78 ± 0.05	24.98 ± 0.05	25.78 ± 0.07
19	57882.35745	26.55 ± 0.07	24.26 ± 0.08	26.21 ± 0.08	57882.43069	25.79 ± 0.09	25.01 ± 0.09	25.98 ± 0.08
20	57901.68632	26.53 ± 0.08	24.26 ± 0.06	26.21 ± 0.08	57901.75265	25.79 ± 0.07	25.02 ± 0.08	25.90 ± 0.06
21	57911.21975	26.52 ± 0.05	24.27 ± 0.04	26.12 ± 0.08	57911.30027	25.78 ± 0.04	24.95 ± 0.05	25.72 ± 0.09
22	57915.85382	26.56 ± 0.06	24.28 ± 0.06	26.11 ± 0.09	57915.91841	25.82 ± 0.07	24.95 ± 0.08	25.81 ± 0.08
23	57925.58697	26.53 ± 0.07	24.26 ± 0.05	25.91 ± 0.05	57925.64973	25.79 ± 0.07	24.97 ± 0.06	25.84 ± 0.09
24	57931.34880	26.52 ± 0.07	24.26 ± 0.05	25.99 ± 0.07	57931.41506	25.78 ± 0.07	25.01 ± 0.06	25.70 ± 0.09
25	57936.61826	26.56 ± 0.05	24.29 ± 0.06	26.04 ± 0.07	57936.73306	25.82 ± 0.07	24.99 ± 0.07	25.67 ± 0.05
26	57946.45948	26.54 ± 0.06	24.27 ± 0.08	26.06 ± 0.07	57946.52410	25.81 ± 0.08	24.97 ± 0.09	25.68 ± 0.08
27	57953.14623	26.55 ± 0.07	24.26 ± 0.05	26.01 ± 0.07	57953.21083	25.81 ± 0.05	25.01 ± 0.06	25.64 ± 0.07
28	57964.26810	26.57 ± 0.06	24.26 ± 0.08	26.04 ± 0.08	57964.33258	25.83 ± 0.08	25.00 ± 0.09	25.69 ± 0.09
29	57971.61629	26.56 ± 0.06	24.30 ± 0.06	26.04 ± 0.07	57971.68077	25.78 ± 0.07	25.01 ± 0.07	25.75 ± 0.09
30	57978.10350	26.56 ± 0.07	24.27 ± 0.04	26.09 ± 0.07	57978.16831	25.82 ± 0.06	24.99 ± 0.05	25.75 ± 0.05
31	57985.54818	26.54 ± 0.07	24.28 ± 0.03	26.33 ± 0.06	57985.61031	25.80 ± 0.05	24.99 ± 0.04	25.72 ± 0.07
32	57993.48529	26.56 ± 0.07	24.28 ± 0.07	26.23 ± 0.08	57993.55398	25.82 ± 0.06	24.99 ± 0.08	25.83 ± 0.10
33	57999.30881	26.55 ± 0.06	24.27 ± 0.05	26.22 ± 0.07	57999.37343	25.81 ± 0.06	24.97 ± 0.06	25.88 ± 0.09
34	58011.35797	26.58 ± 0.05	24.26 ± 0.04	26.23 ± 0.07	58011.42352	25.78 ± 0.07	25.03 ± 0.06	25.78 ± 0.08

Notes: (1) shows the number of observations. (2) and (6) are MJD (Modified Julian Day) times of F606W and F814W observations, respectively. (3), (4), (5), (7), (8) and (9) show F606W and F814W Vega magnitudes of possible optical counterparts, respectively.

**Table 4.** Best sinusoidal fitting parameters of possible optical counterpart C3.

Parameters	Units	F606W	F814W
$P$	Period (days)	124.12 ± 0.27	127.04 ± 2.24
$A$	Amplitude (mag.)	0.16 ± 0.01	0.11 ± 0.02
$\phi$	Phase (°)	217.18 ± 0.11	216.85 ± 0.15
$\bar{m}$	Average magnitude	26.11	25.77
$\chi^2$	Chi-square test	45.99	39.51
$dof$	Number of degrees of freedom	31	31
$\chi^2_\nu$	$\chi^2/dof$	1.48	1.27

found a unique optical counterpart that was not within the error radius derived in this study. In their study, all reference sources were not in the same frame on *HST* images. In addition, all references are not located on the optical axis of the S3 chip of *Chandra* ACIS. Moreover, there is also only 0''.05 offset between the *Chandra* X-ray and *HST* optical coordinates of the ULX-8 which corresponds to just one pixel in the ACS/WFC images. In this study, astrometric errors were calculated more precisely and different from their approach.

In order to search for any optical periodic modulations, 34 *HST* ACS/WFC F606W and F814W observations were used. A  $125.5 \pm 2.3$  d optical periodic modulation was determined for counterpart C3 in the F606W and F814W long-term light-curves with amplitude of  $0.14 \pm 0.02$  mag. at greater than 95% confidence level. No periodic modulation and also no optical variability were observed for remaining counterparts C1 and C2.

The  $\log(F_X/F_X)$  ratios for C1 and C3 were found as  $\sim 2.6$



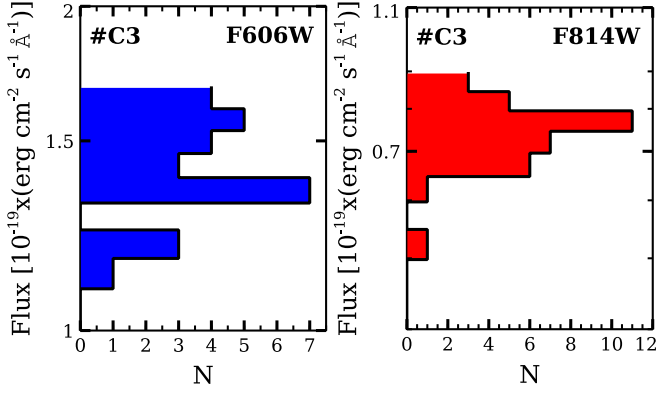


**Figure 8.** The histogram of fluxes F606W (left) and F814W (right) observations for possible counterpart C3. Observations binned with 12 days and N is the number of observations.

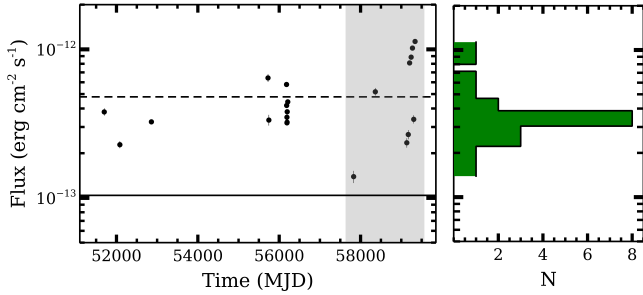


**Figure 9.** The long-term *Chandra* X-ray light-curve of M51 ULX-8 (left) and its histogram (right). The histogram of fluxes was binned with 12 d. N is the number of observations. Dashed and solid black lines indicate the average of the fluxes and the flux threshold for ULX state adopted distance of 9 Mpc, respectively. The gray colored area represents previously unused observations for the ULX-8.

and  $\sim 2.3$  respectively which are in the range of X-ray binaries values. However, it was found as  $\sim 1.6$  for C2 that this value is within the given range for AGNs or BL Lac objects. Therefore, the possibility that the C2 is the optical counterpart of the ULX-8 may be ruled out. However, considering the ULX inclination, we could not know whether a ULX can have  $F_X/F_{\text{optik}}$  in the same range as an AGN. In addition, if these sources are truly the optical counterparts of the ULX-8 and also if the observed X-ray emission comes from the accretion flow, X-ray emission could change on far shorter timescales. Therefore, these ratios calculated from nearly simultaneous observations may be misleading for classifying sources. Since the C3 is almost located in the center of the  $1-\sigma$  (68%) as well as 90% astrometric error radius (see Figure 3) it could be the most likely optical counterpart of the ULX-8. Moreover, the remaining optical counterpart C1 is not completely excluded, but the optical source C3 has various evidence (e.g. X-ray-optical variability) to represent the optical nature of the ULX-8.

The ULX-8 which its compact object well-known to be as a strong neutron star candidate has shown long-term X-ray variability (Brightman et al. 2020). However, there are no reported any period (e.g. spin, orbital or super-orbital) for the M51 ULX-8. The most exciting result

of this study is the detection of an 125.5-d optical periodic modulation for possible optical counterpart C3. Since the orbital period of ULX-8 is unknown, this could be either an orbital period or a super-orbital period. The possible scenarios of the nature of optical periodic variation which are frequently mentioned in the literature are discussed for ULX-8 as follows:

- If a compact object interacted with a disk of a typical Be-X-ray binaries (BeXRBs) donor, the effects observed on the disk (e.g. darkening, rotating density waves) could be cause a super-orbital period (Townsend & Charles 2020). Vasilopoulos et al. (2020) argued that the 38-day super-orbital period discovered for M51 ULX-7 was due to disk precession and they proposed free precession of the NS as a compelling motor to drive disc precession. The super-orbital periods seen in PULXs were correlated to the precession of an accretion disk induced by the Lense–Thirring precession of a large scale-height accretion flow (Middleton et al. 2018, 2019b). In most instances, super-orbital periods could be independently determined from optical light-curves of BeXRBs. When NS passes through around the equatorial disk of the rapidly rotating BeXRB donor, the orbital motion of the NS often causes a small optical flare. Also in this case, due to formation and depletion of disk or rotating density waves could be observed as a super-orbital period (Townsend & Charles 2020). The Be stars generally are massive main-sequence star and the range of orbital periods is (10–300) d with O-A types (Belczynski & Ziolkowski 2009). If the 125.5 day is the orbital period of ULX-8, this scenario can be acceptable for C3. The super-orbital periods are also detected in the long-term X-ray light-curves of ULXs (e.g. NGC 5907 ULX1 Walton et al. 2016 and M51 ULX7 Brightman et al. 2020) however, it was not found for the ULX-8.

- The main problem with identifying the donor star in the optical emission of ULXs is that the optical contribution from the accretion disk, either directly or irradiated, is mostly unknown. In order to identify the possible contribution to the observed optical emission, the SED features of the counterparts were investigated using *HST* optical observations. In most cases, the observed *blackbody* spectrum of the optical emission is a feature of donor stars. On the other hand, if optical emission is mostly dominated by an accretion disk, the optical SED could have a roughly *power-law* spectrum as well as the optical-X-ray variability is also observed (Tao et al. 2011). These are quite consistent only in case C3 since the optical SED for only possible counterpart C3 is adequately fitted with *power-law* ( $\alpha = -2.98 \pm 0.29$ ) at 95% confidence level (Figure 5). Acceptable optical spectral models were not found for the C1 and C2.

Due to the orbital motion of the donor which is distorted by the effects of gravity and is not irradiated equally by the X-ray radiation of the accretion disk, the optical periodic modulation that is not related to the orbital period could be observed. Although strong clues are required to accept the 125.5-day optical variability as a super-orbital period of disk origin, the possibility of this should not be ruled out. If indeed the periodic variability found for C3 is due to the orbital motion of the donor, the spectral type of C3 could not be predicted since the optical emission is dominated by the disk. Observed the X-ray-optical correlated variability could be a direct evidence of the irradiated disk model (Tao et al. 2011; Grisé et al. 2012). In addition, optical variabilities of the Galactic X-ray binaries correlate with the X-ray variabilities (Charles & Coe 2003). Simultaneous X-ray/optical observations are needed to constrain the nature of this variability.

- Double peaked profile (bi-modal distribution) of the light-curves may show evidences of precession of the disk or propeller effect (Tsygankov et al. 2016; Grebenev 2017). However, the propeller regime is related to variabilities in the accretion rate and due to the fact that the observed flux modulation is periodic, it is incomprehensible how changes in the accretion rate can be periodic unless they are related to the binary orbit (Brightman et al. 2019). Allak et al. (2022a) reported an optical periodic variation of 264 d for one of the two optical counterparts of M51 ULX-4 which shows long-term X-ray variability two order magnitudes. In addition, they found some evidence for the existence of a bi-modality distribution of the X-ray flux of ULX-4. As seen in the Figure 8, surprisingly, the observed optical fluxes of the C3 exhibits the bi-modal distribution in both filters which may suggest a link between high X-ray variability while there is no strong evidence of the bi-modality in the X-ray light-curve. Another optical periodic modulation (6.12-day) is discovered by Liu et al. (2009) for the NGC 1313 X-2 which have weak coherent pulsations (Sathyaprakash et al. 2019). This variability was explained as contamination from the X-ray reprocessing in the accretion disk (Liu et al. 2009; Grisé et al. 2012; Zampieri et al. 2012). The scenario suggested for X-2 in which the shape of the optical light curve is similar to case C3 is quite reasonable for C3.

- The CMD, deploying the V-band vs (B-V), was used to estimate the ages of the possible optical counterparts. The CMD of C1 and C3 was displayed in Figure 4. If the optical counterparts of ULX-8 are correlated with their environments, the age of C3 and C1 could be around 18-30 Myr and 90 Myr, respectively. The optical emission of ULXs may come from the accretion disk, either directly or irradiated. Therefore, these possibilities pose a problem for the identification of donor star of ULXs (Allak et al. 2022b). If indeed, the optical emission mostly originate from the disk, the estimated age in case of C3 can be ignored.

- Recently, studies (e.g. Chandar et al. 2020 and Hunt et al. 2021) have suggested that the masses of the optical counterparts could be constrained depending on whether they are detected in the *HST* images. According to their studies, the possible counterparts of ULX-8 could be intermediate-mass X-ray binaries (IMXBs) or high-mass X-ray binaries (HMXBs) since considering the distance (9 Mpc) of galaxy M51, optical counterparts need to have a sufficiently high mass ( $\geq 3 M_{\odot}$ ). On the other hand, it is also possible that the optical counterpart(s) of ULXs could be low mass X-ray binary (LMXB) and could not be detected in the astrometric error radius due to being intrinsically faint at the distance of galaxy M51. In addition, since many ULXs are located inside star forming regions (SFR). Since the SFR strongly dominates over the stellar mass, counterpart(s) might not be detected. Moreover, some ULXs are located in very dense gas and dust and also background level is very high for many galaxies therefore, even if ULXs have optical counterpart(s) they may not be detected.

## ACKNOWLEDGEMENTS

I would like to thank A. Akyuz for her valuable contributions and suggestions. The author gratefully thank to the Referee for the constructive comments and recommendations which help to improve the readability and quality of the paper. I would also like to thank my son Atlas ALLAK who is the sweetest source of my motivation.

## DATA AVAILABILITY

The scientific results reported in this article are based on archival observations made by the *Chandra*<sup>1</sup> and the NASA/ESA Hubble Space Telescope and obtained from the data archive at the Space Telescope Science Institute<sup>2</sup>

## REFERENCES

- Allak S., et al., 2022a, *MNRAS*, **510**, 4355  
 Allak S., Akyuz A., Sonbas E., Dhuga K. S., 2022b, *MNRAS*, **515**, 3632  
 An T., Baan W. A., Wang J.-Y., Wang Y., Hong X.-Y., 2013, *MNRAS*, **434**, 3487  
 An T., Lu X.-L., Wang J.-Y., 2016, *A&A*, **585**, A89  
 Bachetti M., et al., 2014, *Nature*, **514**, 202  
 Begelman M. C., King A. R., Pringle J. E., 2006, *MNRAS*, **370**, 399  
 Belczynski K., Ziolkowski J., 2009, *ApJ*, **707**, 870  
 Bressan A., Marigo P., Girardi L., Salasnich B., Dal Cero C., Rubele S., Nanni A., 2012, *MNRAS*, **427**, 127  
 Brightman M., et al., 2018, *Nature Astronomy*, **2**, 312  
 Brightman M., et al., 2019, *ApJ*, **873**, 115  
 Brightman M., et al., 2020, *ApJ*, **895**, 127  
 Caballero-García M. D., Belloni T., Zampieri L., 2013, *MNRAS*, **436**, 3262  
 Carpano S., Haberl F., Maitra C., Vasilopoulos G., 2018, *MNRAS*, **476**, L45  
 Chandar R., Johns P., Mok A., Prestwich A., Gallo E., Hunt Q., 2020, *ApJ*, **890**, 150  
 Charles P. A., Coe M. J., 2003, arXiv e-prints, [pp astro-ph/0308020](https://arxiv.org/abs/ppastro-ph/0308020)  
 Colbert E. J. M., Mushotzky R. F., 1999, *ApJ*, **519**, 89  
 De Marco B., Ponti G., Miniutti G., Belloni T., Cappi M., Dadina M., Muñoz-Darias T., 2013, *MNRAS*, **436**, 3782  
 Drave S. P., Clark D. J., Bird A. J., McBride V. A., Hill A. B., Sguera V., Scaringi S., Bazzano A., 2010, *MNRAS*, **409**, 1220  
 Earnshaw H., 2020, Searching for transient propeller-phase neutron star ULXs, Chandra Proposal ID #22400554  
 Fabrika S., Ueda Y., Vinokurov A., Sholukhova O., Shidatsu M., 2015, *Nature Physics*, **11**, 551  
 Fürst F., et al., 2016, *ApJ*, **831**, L14  
 Gladstone J. C., Copperwheat C., Heinke C. O., Roberts T. P., Cartwright T. F., Levan A. J., Goad M. R., 2013, *ApJS*, **206**, 14  
 Grebenev S. A., 2017, *Astronomy Letters*, **43**, 464  
 Grisé F., Kaaret P., Corbel S., Feng H., Cseh D., Tao L., 2012, *ApJ*, **745**, 123  
 Heida M., Jonker P. G., Torres M. A. P., Roberts T. P., Walton D. J., Moon D. S., Stern D., Harrison F. A., 2016, *MNRAS*, **459**, 771  
 Hunt Q., Gallo E., Chandar R., Johns Mulia P., Mok A., Prestwich A., Liu S., 2021, *ApJ*, **912**, 31  
 Israel G. L., et al., 2017a, *Science*, **355**, 817  
 Israel G. L., et al., 2017b, *MNRAS*, **466**, L48  
 Joye W. A., Mandel E., 2003, in Payne H. E., Jedrzejewski R. I., Hook R. N., eds, *Astronomical Society of the Pacific Conference Series Vol. 295, Astronomical Data Analysis Software and Systems XII*. p. 489  
 Kaaret P., Ward M. J., Zezas A., 2004, *MNRAS*, **351**, L83  
 Kaaret P., Feng H., Wong D. S., Tao L., 2010, *ApJ*, **714**, L167  
 Kaaret P., Feng H., Roberts T. P., 2017, *ARA&A*, **55**, 303  
 Kong L.-D., et al., 2022, *ApJ*, **933**, L3  
 Liu J.-F., Bregman J. N., Seitzer P., 2002, *ApJ*, **580**, L31  
 Liu J., Bregman J. N., McClintock J. E., 2009, *ApJ*, **690**, L39  
 Lomb N. R., 1976, *Ap&SS*, **39**, 447  
 López K. M., Heida M., Jonker P. G., Torres M. A. P., Roberts T. P., Walton D. J., Moon D. S., Harrison F. A., 2020, *MNRAS*, **497**, 917  
 Maccacaro T., et al., 1982, *ApJ*, **253**, 504  
 Middleton M. J., Walton D. J., Fabian A., Roberts T. P., Heil L., Pinto C., Anderson G., Sutton A., 2015, *MNRAS*, **454**, 3134  
 Middleton M. J., et al., 2018, *MNRAS*, **475**, 154

<sup>1</sup> <https://cda.harvard.edu/chaser/>

<sup>2</sup> <https://mast.stsci.edu/portal/Mashup/Clients/Mast/Portal.html>

- Middleton M. J., Brightman M., Pintore F., Bachetti M., Fabian A. C., Fürst F., Walton D. J., 2019a, *MNRAS*, **486**, 2
- Middleton M. J., Fragile P. C., Ingram A., Roberts T. P., 2019b, *MNRAS*, **489**, 282
- Middleton M. J., Higginbottom N., Knigge C., Khan N., Wiktorowicz G., 2022, *MNRAS*, **509**, 1119
- Miller J. M., Fabian A. C., Miller M. C., 2004, *ApJ*, **614**, L117
- Motch C., Pakull M. W., Soria R., Grisé F., Pietrzyński G., 2014, *Nature*, **514**, 198
- Patruno A., Zampieri L., 2008, *MNRAS*, **386**, 543
- Poutanen J., Lipunova G., Fabrika S., Butkevich A. G., Abolmasov P., 2007, *MNRAS*, **377**, 1187
- Roberts T. P., 2007, *Ap&SS*, **311**, 203
- Rodríguez Castillo G. A., et al., 2020, *ApJ*, **895**, 60
- Sathyaprakash R., et al., 2019, *MNRAS*, **488**, L35
- Scargle J. D., 1982, *ApJ*, **263**, 835
- Sirianni M., et al., 2005, *PASP*, **117**, 1049
- Song X., Walton D. J., Lansbury G. B., Evans P. A., Fabian A. C., Earnshaw H., Roberts T. P., 2020, *MNRAS*, **491**, 1260
- Soria R., Cropper M., Pakull M., Mushotzky R., Wu K., 2005, *MNRAS*, **356**, 12
- Stetson P. B., 1987, *PASP*, **99**, 191
- Stoeckle J. T., Morris S. L., Gioia I. M., Maccacaro T., Schild R., Wolter A., Fleming T. A., Henry J. P., 1991, *ApJS*, **76**, 813
- Sutton A. D., Roberts T. P., Walton D. J., Gladstone J. C., Scott A. E., 2012, *MNRAS*, **423**, 1154
- Sutton A. D., Done C., Roberts T. P., 2014, *MNRAS*, **444**, 2415
- Swartz D. A., Soria R., Tennant A. F., Yukita M., 2011, *ApJ*, **741**, 49
- Tao L., Feng H., Grisé F., Kaaret P., 2011, *ApJ*, **737**, 81
- Terashima Y., Inoue H., Wilson A. S., 2006, *ApJ*, **645**, 264
- Townsend L. J., Charles P. A., 2020, *MNRAS*, **495**, 139
- Tsygankov S. S., Mushtukov A. A., Suleimanov V. F., Poutanen J., 2016, *MNRAS*, **457**, 1101
- Urquhart R., Soria R., Johnston H. M., Pakull M. W., Motch C., Schwope A., Miller-Jones J. C. A., Anderson G. E., 2018, *MNRAS*, **475**, 3561
- Vasilopoulos G., Lander S. K., Koliopanos F., Bailyn C. D., 2020, *MNRAS*, **491**, 4949
- Vaughan S., Uttley P., Markowitz A. G., Huppenkothen D., Middleton M. J., Alston W. N., Scargle J. D., Farr W. M., 2016, *MNRAS*, **461**, 3145
- Walton D. J., et al., 2014, *ApJ*, **793**, 21
- Walton D. J., et al., 2016, *ApJ*, **827**, L13
- Walton D. J., et al., 2018, *ApJ*, **857**, L3
- Yao Y., Feng H., 2019, *ApJ*, **884**, L3
- Zampieri L., Impiombato D., Falomo R., Grisé F., Soria R., 2012, *MNRAS*, **419**, 1331

This paper has been typeset from a  $\text{\LaTeX}$  file prepared by the author.